1   **Copper and Cobalt Improve the Acid Resistance of Alkali-Activated Cements**

2   *Juan Pablo Gevaudan [1], Alejandro Caicedo-Ramirez [1], Mark Hernandez[1], Wil V. Srubar III [1†]*

3   [1]Department of Civil, Environmental, and Architectural Engineering, University of Colorado Boulder,

4   Boulder, Colorado USA. [†]Corresponding Author 1111 Engineering Drive, ECOT 441 UCB 428, Boulder,

5   Colorado USA 80309. T +1 303 492 2621, E: wsrubar@colorado.edu

6   **Abstract**

7   Experimental evidence of a new acid degradation mechanism in alkali-activated cements (AACs) micro-

8   doped with copper (Cu) and cobalt (Co) is presented in this work. Cu and Co incorporation into binary

9   metakaolin and basic oxygen furnace (BOF) slag-based AACs reduced bulk permeable porosity and acid

10   penetration and retarded the formation of calcium sulfate phases upon exposure to acid. Analysis of

11   microstructural evolution and elemental mobility using X-ray diffraction and electron microprobe

12   analysis (EMPA) showed that Cu and Co doping was associated with major differences in AAC leaching

13   patterns when exposed to sulfuric acid. Converging lines of evidence suggest that acid resistance is

14   improved by the preferential mobilization of Cu and Co, along with other multivalent cations (i.e.,

15   magnesium), at the acid degradation front(s), stabilizing the AAC binder and inhibiting further

16   deterioration.

1. Introduction

17   **1. Introduction**

18   Unanticipated microbial-induced concrete corrosion (MICC) continues to challenge the underground

19   conduit networks that make up an important part of urban infrastructure. One of the most aggressive and

20   ubiquitous forms of MICC stems from the biologically mediated production of sulfuric acid in sewers.

21   Population centers around the world share this serious and growing problem [1]. In the United States,

22   local governments spend approximately $50 billion in the construction, operation, and maintenance of

23   over 800,000 miles of sewers annually [2], [3]. In order to rehabilitate and expand the wastewater

24   infrastructure, the United States Environmental Protection Agency estimates that $271 billion is needed

25   over the next generation, a substantial fraction of which is dedicated to directly respond to widespread

26   biogenic corrosion that is significantly reducing the service life of buried sewers [3], [4]. Sewer service

27   life reductions result from the fact that conventional ordinary portland cement (OPC) concrete is rapidly

28   compromised by biogenic sulfuric acid attack, producing gypsum and amorphous silica from the

29   cementitious binder [1], [5]. The non-load bearing quality of gypsum leads to severe structural

30   deterioration and, ultimately, pipe failure [5], [6], [7].

31   Mitigation strategies for microbial-induced concrete corrosion are often short-term, relatively expensive,

32   and site-limited. In order to provide *in-situ* acid protection for OPC concrete sewers, operators have used

33   surface coatings and linings, concrete binder additives, and, even, antimicrobial additives [8]–[10]. As an

34   example, a popular mitigation practice includes the use of acid resistant, cured-in-place resins. While

35   seemingly effective in resisting acid exposure, the associated cost of these materials is high ($390-900 per

36   linear meter), they require special curing conditions, and may not prevent corrosive gas infiltration,

37   seriously compromising the effectiveness of this mitigation practice [11]. Further, with the exception of

38   antimicrobial additives, these mitigation strategies do not address one of the underlying causes of MICC

39   in these environments: acidophilic microbial growth. As a result, this study has focused on the

40   incorporation of biocidal metals that, in micromolar concentrations, can function as antimicrobial agents

41   into an alkali-activated cement (AAC), an acid-resistant alternative to OPC [10], [12].

42   *1.1 Alkali-activated cements and acid durability*

43   A growing cohort of researchers has shown that AACs can provide better acid resistance compared to

44   OPC. Acid resistance in AACs is dependent on a number of physical and chemical factors, including acid

45   type, concentration, activity, and the AACs' chemical composition [13]–[17]. Increased acid resistance

46   has been attributed to the formation of decalcified and modified aluminosilicate gel upon exposure to acid

47   [18]–[23], which has been shown to delay the acid degradation process [18].

48   Deterioration of AACs exposed to strong acids initiates *via* exchange between interlayered alkali cations

49   (Na^+, K^+, Ca^{+2}, Mg^{+2}) and hydronium ions (H_3O^+) [24]. This exchange leads to destabilization of the

50   aluminosilicate framework, resulting in electrophilic attack of Si-O-Al bonds and the formation of Si-OH

51   and Al-OH groups [22]. While Si-OH compounds are believed to form an amorphous silica with some

52   beneficial properties [13], [14], [18], the formation of Al-OH results in dealumination of the

53   aluminosilicate binder [13], [14]. Initial cation exchange leads to decalcification of the cementitious

54   binder and formation of soluble salts, namely calcium acetate when exposed to acetic acid or gypsum

55   when exposed to sulfuric acid [18]. In addition to soluble products, fissure cracks are formed likely due to

56   destabilization of the aluminosilicate framework, which results in a loss of mechanical integrity [22].

57   *1.2 Scope of Work*

58   Motivated by previous work related to antimicrobial metals [25] and acid-resistant AACs, the aim of this

59   study was to experimentally investigate the effect of incorporating micro-doses of heavy metals, namely

60   copper (Cu) and cobalt (Co), on the acid resistance of AACs. Three samples of binary metakaolin- and

61   metal-doped basic oxygen furnace (BOF) slag-based AACs were prepared and exposed to sulfuric acid.

62   Acid exposure was correlated with changes in mineralogy, chemical composition, and physical properties,

63   including bulk permeable porosity and acid corrosion depth. Microstructural evolution and elemental

64   mobility were also investigated *via* X-ray diffraction and electron microprobe analysis (EMPA),

65   respectively, after semi-dynamic leaching in sulfuric acid solutions.

2. Materials and Experimental Methods

67   *2.1 Materials*

68   Basic oxygen furnace slag (BOF-S), obtained from the Indiana Harbor East Steel Mill complex (Indiana,

69 USA), and Metakaolin (MK) (MetaMax), supplied by BASF Chemical Corporation (Georgia, USA),

70 were used as aluminosilicate precursors for alkali-activation. $Cu(NO_3)_2$ (99% purity, Acros Organics) and

71 $Co(NO_3)_2$ (99 % purity, Acros Organics) were both utilized to adsorb heavy metals onto the BOF-S

72 precursor.

73 ***2.2 Experimental Methods***

74 *2.2.1 Copper (Cu) and Cobalt (Co) adsorption*

75 Batch heavy metal (i.e., Cu, Co) adsorption onto BOF-S was performed as follows. First, 10 g of

76 $Cu(NO_3)_2$ were added to one liter of deionized water until completely dissolved. Next, 50 g of slag (Sieve

77 No.20: 841 μm) were added to the solution and mixed overnight at 150 rpm and room temperature. After

78 this process, the Cu-laden slag (Cu-S) was separated from the solution using qualitative filter paper (No.1,

79 Whatman), rinsed with water to remove any unattached particles, and oven dried at 40°C. A similar

80 procedure was performed to create the same material which was laden with Cu and Co (Cu/Co-S);

81 however, in addition to $Cu(NO_3)_2$, 10 g/L of $Co(NO_3)_2$ were dissolved in the initial solution prior to slag

82 addition. Next, the BOF-S was ground in mill capsules with clean, packed yttrium-stabilized zirconium

83 grinding beads (American Elements) using a McCrone micronizing mill. A No.100 sieve was used to

84 ensure a sub-149 μm particle size.

85   **Table 1** shows the chemical composition of all AAC precursors (MK, BOF-S, Cu-S, and Cu/Co-S)

86 determined by ICP-OES, on a calibrated ARL 3410+, using modifications to a widely accepted technique

87 developed by Farrell et al. [26]. Five mL of a 7:3 mixture of hydrochloric acid and hydrofluoric acid

88 were combined with 2 mL of nitric acid and placed in digestion tubes that were maintained at 95°C in a

89 digestion block (HotBlock, Environmental Express) for approximately two hours. Samples were then

90 cooled and brought to 50 mL with a 1.5% boric acid solution (by mass). The samples were then reheated

91 to 95°C for 15 minutes and cooled for analysis. The samples were diluted 10x with deionized water and

92 analyzed with an ICP-OES, as described above. An analytical blank, along with three standards that were

93 made by accurately diluting certified standards, was used for calibration. A basaltic internal standard

94 (Valmont Dike, Colorado USA) of known chemical composition was digested and analyzed to ensure the

95 accuracy of the chemical composition results shown in **Table 1**. Precursors were supplemented using a

96 reagent-grade sodium silicate (NaSi) solution supplied by Sigma-Aldrich. The chemical composition of

97 the NaSi solution was determined to have a SiO_2:Na_2O molar ratio of 2.5 (SiO_2 = 27 wt.%, Na_2O = 11

98 wt.%, H_2O = 62 wt.%), as obtained *via* ICP-OES as previously described.

99 **Table 1.** Chemical composition of MK, BOF-S, Cu-S, and Cu/Co-S in weight percent.

Precursor	SiO_2	Al_2O_3	CaO	SO_4	Fe_2O_3	K_2O	Na_2O	MgO	MnO	Cu	Co	P_2O_5
MK	52.1	41.3	0.07	0.3	0.36	0.11	0.33	-	-	-	-	0.08
BOF-S	14.7	6.6	31.7	0.4	25.8	<0.05	0.1	10.8	2.5	-	-	0.7
Cu-S	14.4	7.4	29.1	0.3	24.2	<0.05	0.1	10.7	2.6	2.4	-	0.1

Cu/Co-S	13.6	6.7	28.9	0.2	26.3	<0.05	0.1	6.5	2.4	1.5	1.3	0.7

100

101   *2.2.2 AAC sample preparation*

102   In this study, AACs were prepared by mixing 66% MK and 33% BOF-S by weight with NaSi solution

103   according to the prescribed mix design parameters shown in **Table 2**. All materials were mixed at room

104   temperature using a Waring PDM112 mixer. To ensure no material residual remained on the sides of the

105   vessel, the mixing procedure was repeated twice: one minute of manual mixing, followed by one minute

106   of mechanical mixing. Samples were then cured inside hermetically sealed plastic containers for 72 ±1

107   hours at 100% relative humidity and 22°C. The constant humidity chamber was prepared according to

108   ASTM E104 by placing a supersaturated salt solution of sodium phosphate (Sigma-Aldrich) inside the

109   plastic containers. After this period, both samples were cured inside a Quincy forced air laboratory oven

110   set to 20°C for 25.5 ± 1.5 hours.

111   Paste samples were cast in both small cylinder molds (diameter 2.4 cm, height 1.5 cm) used for semi-

112   dynamic leaching experiments (see Section 2.2.2) and longer cylinder molds (diameter 1.4 cm, height 4

113   cm) that were used to determine acid corrosion depth (see Section 2.2.7).

114   **Table 2.** Sample classification and mixture proportions for MK-BOF-S AACs. Important parameters are

115   reported in molar atomic ratios (Si:Al, Na:Al) and molecular ratios ($H_2O:Al_2O_3$).

Mixtures	Solids		Alkali-Activating Solution	Important Parameters		
	MK (g)	Slag (g)	Sodium Silicate (ml)	Si:Al	Na:Al	$H_2O:Al_2O_3$
Control	80	40	122	2.0	0.8	15
Control + Cu	80	40	122	2.0	0.8	15
Control + Cu/Co	80	40	122	2.0	0.8	15

116   *2.2.3 Semi-Dynamic Leaching*

117   Cast samples (diameter 2.4 cm, height 1.5 cm) were placed in polypropylene plastic containers with either

118   sulfuric acid solution (1% v/v) or deionized water at a volume-to-surface area ratio of 10, as described by

119   ASTM C1308. In addition, samples were suspended by triangle plastic stands to allow full surface

120   exposure to the acidic medium. Exposure media was replaced daily for seven consecutive days for each

121   of the three replicates. Samples of leachate media were taken before each replacement. Prior to

122   characterization, samples were dehydrated by solvent exchange with anhydrous ethanol (200 proof, 0%

123   H_2O, Decon Labs) and dried at 40°C overnight in a Quincy forced air laboratory oven [27]. Leachate

124   media samples were analyzed with ICP-OES and ICP-MS.

125   *2.2.4 Desorption potential and acid neutralization capacity*

126   Cured AAC specimens were crushed using a mortar and pestle to pass a No. 100 mesh sieve (< 149 μm).

127   Solutions containing deionized water and H_2SO_4 (97% w/w) were prepared to establish a concentration

128   gradient of H_3O^+ (expressed as equivalents of acid per kg of AAC). The powdered specimens were added

129   to the solutions at a liquid-to-solid ratio of 20. Portions of powdered specimens for all three AAC samples

130   were chemically characterized *via* ICP-OES to determine an initial concentration of elements. Batches

131   were mixed overnight at 150 rpm and room temperature. Final pH of the solutions was measured and

132   batches were then centrifuged at 5000 rpm for 10 minutes. The supernatant was analyzed for soluble

133   cations using ICP-OES and the solid was oven dried at 40°C and analyzed for their mineral profiles on a

134   Siemens D500 X-ray diffractometer. The initial chemical compositions of the powders were compared

135   with the chemical compositions of the supernatant after batch reactions to calculate a leached percentage

136   of each element (Si, Al, Na, Ca, Mg, Fe, Cu and Co) with respect to the total initial mass of each.

137   *2.2.5 X-ray diffraction (XRD)*

138   To determine mineralogy, AAC samples were first crushed into a powder with a mortar and pestle. The

139   powder was then prepared for analysis using a modified method based on [28]. The former method was

140   modified to employ corundum as an internal standard instead of zincite. A Siemens D500 X-ray

141   diffractometer was used to acquire energy dispersion patterns for all samples. Samples were analyzed

142   from 5 to 65 degrees 2θ using Cu Kα X-ray radiation, with a step size of 0.02 degrees and a dwell time of

143   2 seconds per step. Mineralogy was identified using Jade software (MDI, Version 9) and the International

144   Centre for Diffraction Data (ICDD) 2003 database. Corundum was used to normalize peak heights

145   between samples and align diffraction patterns.

146   *2.2.6 Bulk Permeable Porosity*

147   Permeable porosities were measured using a vacuum saturation method, which was selected because it

148   has improved efficiency compared to conventional laboratory methods for estimating permeable porosity

149   [29]. The method was modified by using anhydrous ethanol in lieu of water to prevent any hydration

150   reactions from occurring during the analysis. Sample volumes were observed by measuring sample

151   dimensions with calibrated micro-calipers and vacuum-saturated with ethanol for 24 hours. The saturated-

152   surface-dry (SSD) weight was recorded using a Mettler Toledo PL 1502E scale after ethanol-vacuum

153   immersion. Samples were then dried at 40°C for 24 hours and their oven-dry (OD) weights were

154   recorded. Permeable porosity was calculated as the difference in SSD mass and OD mass normalized by

155   the density of ethanol (0.803 g/cm^3) all divided by total sample volume.

156   *2.2.7 Corrosion Depth*

157   Cast cylindrical samples (diameter 1.4 cm, height 4 cm) were wrapped with commercial electrical tape

158   twice at both the curved and bottom surfaces of the cylinder, leaving only one circular face exposed.

159   Samples were submerged in sulfuric acid solution (1% v/v) at a volume-to-surface ratio of 30 to

160   determine corrosion depth in one dimension. After acid exposure, samples were dehydrated by immersion

161   in anhydrous ethanol (200 proof, Decon Labs) and dried at 40°C overnight in a Quincy forced air

162   laboratory oven [27]. The corrosion layer was qualitatively identified by obvious color change and

163   corrosion depths were quantitatively measured using calipers as previously described. The weak product

164   layer was evaluated by measuring the total height dimension of the sample before and after brushing with

165   a commercial copper wire brush until no additional residue detached from the material.

166   *2.2.8 Electron Micro-Probe Analysis (EMPA)*

167   The mobility and fate of elements of interest before and after exposure to sulfuric acid were analyzed by

168   compiling X-ray element maps of Si Kα, Al Kα, S Kα, Ca Kα, Na Kα, Fe Kα, Mg Kα, Co Kα, and Cu

169   Kα, which were obtained using a JEOL-8230 electron microprobe. In some cases, two maps for Cu Kα

170   were aggregated to enhance precision. An acceleration voltage of 15 keV and beam current of 100 nA

171   was used for all maps. The electron beam was defocused to 5-6 μm to match the pixel size, and a dwell

172   time of 20 msec was used. Element maps were treated with CalcImage (ProbeSoftware, Inc.) to remove

173   the background using the mean atomic number background correction, and a matrix correction was

174   additionally performed as required for quantitative work [30], [31]. Raw data, expressed as net counts, are

175   semi-quantitative, since each pixel likely represents a mixture of two or more phases. Considering these

176   material limitations, atomic percentages were quantified to discern the central tendencies of bulk Si:Al

177   ratios using statistical analysis. EMPA data were analyzed for statistical significance by utilizing Minitab

178   18.1 statistical analysis software. The respective intensity scale bars, which differ for each element, are

179   presented in the **Supplementary Information**.

180   **3. Experimental Results**

181   ***3.1 Dissolution behavior of AACs***

182   *3.1.1 Semi-dynamic time-dependent leaching*

183   The time-dependent leaching behaviors of all samples exposed to deionized water are shown in **Figure 1.**

184   Elemental leaching decreases with exposure time in all samples and for all elements. Under this scenario,

185   the elements which dominated leaching on a molar basis were silicon (Si) and sodium (Na), while

186   concentrations of other elements were either not present or were below the method detection limit. For

187   example, the Si leaching in the Control sample, on the order of 7.4 mg/cm^2 in the first day, decreased

188   68% by the second day. No other evidence of elemental leaching was observed.

189   Formulations containing copper (Cu) and cobalt (Co) exhibited higher normalized leaching of both Si

190   and Na in deionized water (**Figure 1**). The addition of Cu and Co increased the leaching of Si by a factor

191   of approximately 3.4 when compared to the Control. While Na ions exhibit similar leaching behavior as

192   Si ions in all samples, the addition of Cu and Co effectively doubled the Na leaching output in

193   comparison to the Control.

194   As shown in **Figure 1**, acid exposure induces elemental mobility in the AAC matrix, but samples

195   containing Cu and both Cu and Co leach lower amounts of iron (Fe), magnesium (Mg), aluminum (Al),

196   and calcium (Ca) than the Control. While Na leaching does not differ between samples, leaching of Ca in

197   the samples containing Cu is lower than the Control after the first day of acid exposure. Similarly, the

198   leaching of the samples containing Cu is lower than that of the Control for Fe, Mg, Si, and Al ions after

199   one day of exposure. The leaching profile from AAC samples containing both Cu and Co is also lower

200   after the second day of acid exposure with respect to Fe, Mg, and Al ions.

201
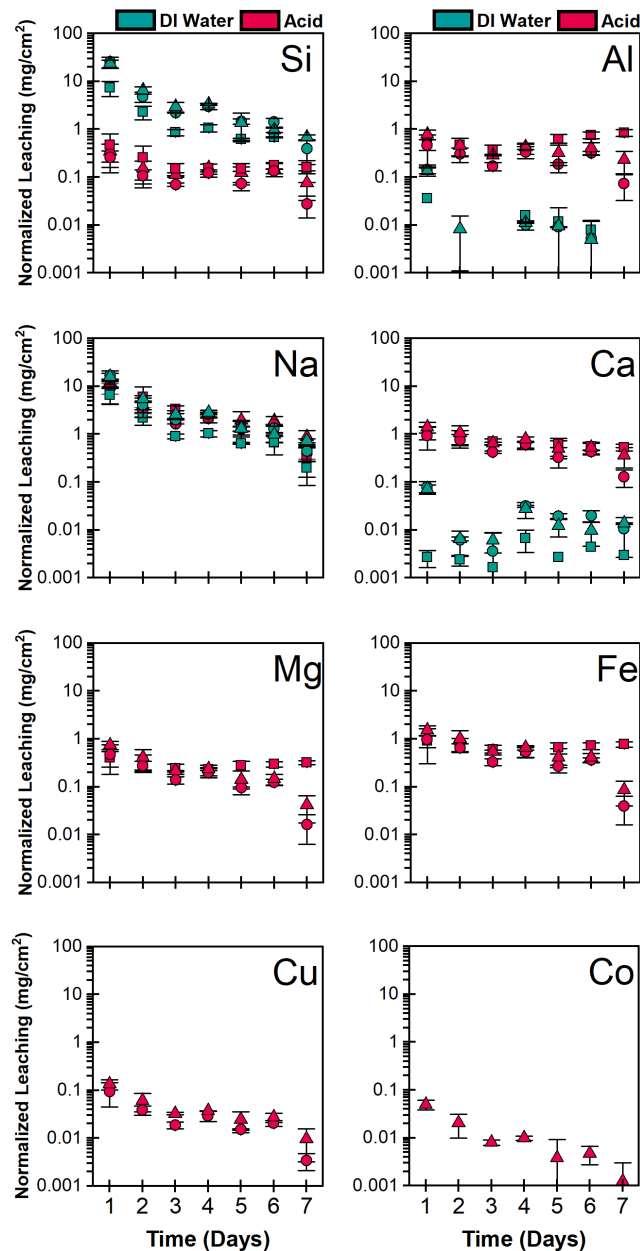
202

203   **Figure 1.** Surface area-normalized daily elemental leaching (mg/cm^2) in deionized water (DI water) and

204   sulfuric acid (Acid) over seven days for Control (□), Control + Cu (○), and Control + Cu/Co (△). Error

205   bars represent the standard deviation of three replicates.

206   *3.1.2 Desorption potential and acid neutralization capacity*

207   From leaching profiles shown in **Figure 2**, it is evident that all formulations liberated increasing

208   quantities of chemical constituents in response to acid exposure (with the exception of Si). The results

209   suggest that cations can be grouped based on the difference between the percentage leached at 8 eq/kg of

210   acid exposure and the percentage leached at the baseline condition (0 eq/kg of acid exposure): (1) mildly

211   affected (< 20% difference) by acid addition (Ca, Si, Al) and (2) strongly affected (> 20% difference) by

212   acid addition (Mg, Na, Fe, Cu, Co). Leached Ca increases from nondetectable to a stable magnitude of

213   approximately 16% when acid exposure was above 4 eq/kg. Si and Na were the only cations leached in

214   the absence of acid. However, net Si leaching declined in response to increasing acid exposures, while Na

215   plateaued at 90% at or above 6 eq/kg acid exposure. Al was detected at and above 6 eq/kg acid exposure,

216   with a maximum leaching of 15% at 8 eq/kg acid exposure. Additionally, Mg and Fe gradually increased

217   presence in response to increasing acid exposures to their respective maxima of 84% and 68% when acid

218   exposure conditions were 8 eq/kg. Cu and Co gradually increase their presence in the leachates as well;

219   these metals were not detectable in the absence of acid but equilibrated at approximately 98% in the

220   leachate at and above 6 eq/kg acid exposure.
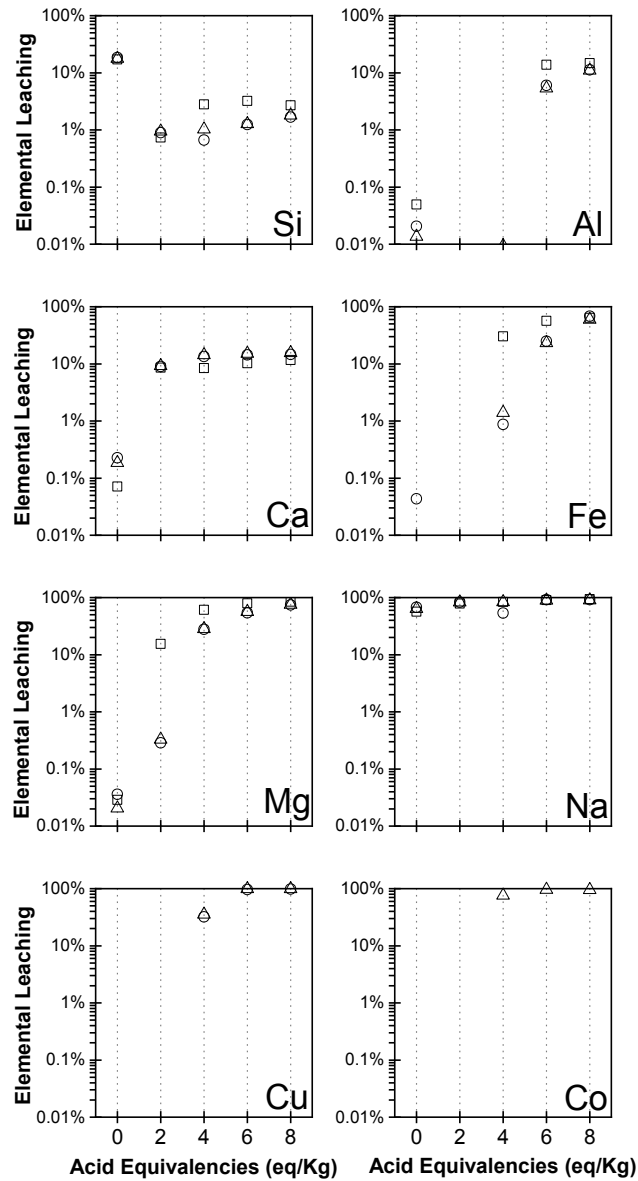
221

222 **Figure 2.** Elemental leachin from pulverized AAC formulations in response to increasing acid

223 concentration (eq H_3O^+/kg AAC) for Control (□), Control + Cu (○), and Control + Cu/Co (△) samples.

224 The pH at the end of these experiments indicated the neutralization capacity of the different AAC

225 formulations. As seen in **Table 3**, no significant differences are observed between formulations. pH

226 values decreased in response to acid addition to pH 2 in an 8 eq/kg acid solution in all sample

227 formulations.

228 **Table 3.** Batch solution pH after 24 hours of acid exposure at 1:20 solid-to-liquid ratio.

	0 eq/kg	2 eq/kg	4 eq/kg	6 eq/kg	8 eq/kg
Control	11.44	9.64	5.32	3.34	2.17
Control + Cu	11.39	9.65	5.23	3.33	2.23
Control + Cu/Co	11.39	9.64	5.02	3.21	2.08

229   ***3.2 Mineralogy***

230   *3.2.1 Mineralogical response of bulk AACs upon acid exposure*

231   **Figure 3** shows mineralogical profiles of the cast (bulk) AAC samples after exposure to different

232   environmental conditions, including sulfuric acid. Salient minerals identified with XRD are listed in

233   **Table 4** with the corresponding unit geometry, volume, and density, as determined by each reference

234   standard. Symbols correspond to the peaks identified in **Figure 3**.

235   Alkali activation of the Control formulation resulted in a cementitious material with traces of the

236   original mineral composition. Minor mineralogical differences between the raw BOF-S, Cu-S, and

237   Cu/Co-S precursors were initially detected (data not shown; see **Supplementary Information**). After

238   alkali-activation, traces of quartz, srebrodolskite, merwinite, and wüstite present in the original BOF-S

239   precursor were detected. Data indicate complete reaction of belite, which resulted in the formation of

240   calcium silicate hydrate (C-S-H) phases in all cement samples.

241   No significant mineral changes were observed between dehydrated AAC samples (**Figure 3a**),

242   samples at ambient conditions (**Figure 3b**), or samples exposed to deionized water (**Figure 3c**).

243   Following exposure to sulfuric acid, however, samples containing Co and Cu had notably lower gypsum

244   content compared to the Control (**Figure 3d**). However, the acid-exposed Control containing Cu and or

245   Co showed traces of calcium sulfate hydrate (**Table 4**), a similar mineral, with a larger unit cell volume

246   and lower density.

247

248   **Table 4.** Summary of observed minerals as determined by XRD. Mineral shapes, unit volumes, and

249   densities were obtained using the Jade5 mineral database as a reference standard.

Mineral Name	Stoichiometry	Symbol	Unit Geometry	Unit Cell Volume ($Å^3$)	Density (g/cm^3)	PDF #
Srebrodolskite	$Ca_2Fe_2O_5$	S	Orthorhombic	448	4.04	00-038-0408
Wüstite	$Fe_{0.9536}O$	W	Cubic	78.5	5.613	01-074-1880
Merwinite	$Ca_3Mg(SiO_4)_2$	M	Monoclinic	659.3	3.15	00-035-0591
Quartz	SiO_2	Q	Hexagonal	113	2.66	00-046-1045
Calcium Silicate Hydrate	$Ca_{1.55}SiO_3 \cdot x(H_2O)$	C	-	-	-	00-033-0306
Calcium Sulfate Hydrate	$CaSO_4 \cdot 0.62(H_2O)$	H	Hexagonal	2,119.90	0.115	00-041-0225
Gypsum	$CaSO_4 \cdot 2(H_2O)$	G	Monoclinic	495.4	2.32	00-033-0311
Corundum	Al_2O_3	O	-	253.54	3.98	00-010-0173
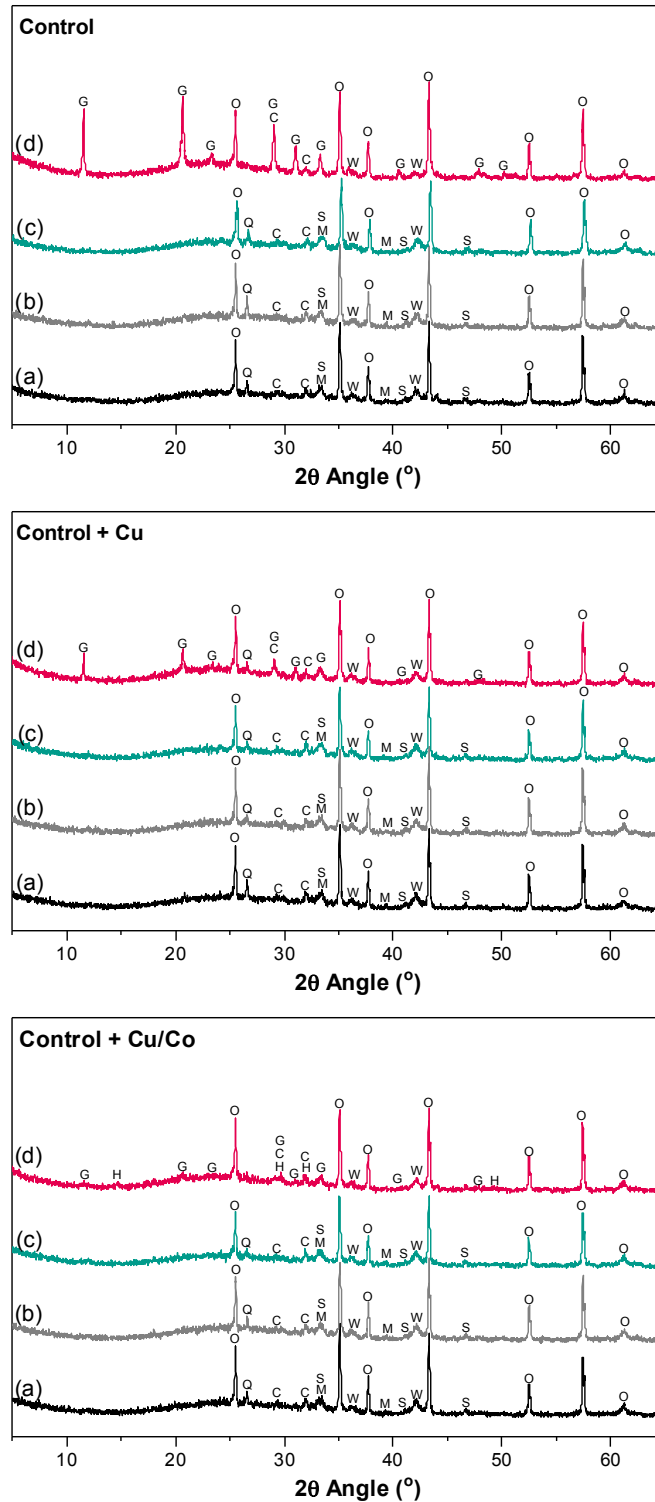
Figure 3. XRD patterns for (a) dehydrated samples, and samples exposed to: (b) ambient conditions (22°C and 30% relative humidity), (c) deionized water, and (d) sulfuric acid. S: srebrodolskite, G: gypsum, H: calcium sulfate hydrate, C: calcium silicate hydrate (C-S-H), W: wüstite, Q: quartz, M: merwinite, and O: corundum.

254 *3.2.2   Mineralogical response of powdered AACs upon acid exposure*

255 As judged by acid equivalents, acid strength affected the formation of gypsum and other minerals (**Figure**

256 **4**) in powderized samples. As discussed, powdered samples were used in conjunction with cast (bulk)

257 samples to explicitly study element liberation and mineral formation and identify changes in mineralogy

258 in response to acid strength. AAC powders exposed to sulfuric acid formed gypsum when acid additions

259 were greater than 4 eq/kg, with minimal changes in the diffraction intensity of gypsum noted in response

260 to increased acid strength. Results of AAC powders exposed to deionized water (**Figure 4a**) indicate the

261 presence of both quartz and srebrodolskite, further substantiating the results obtained and shown in
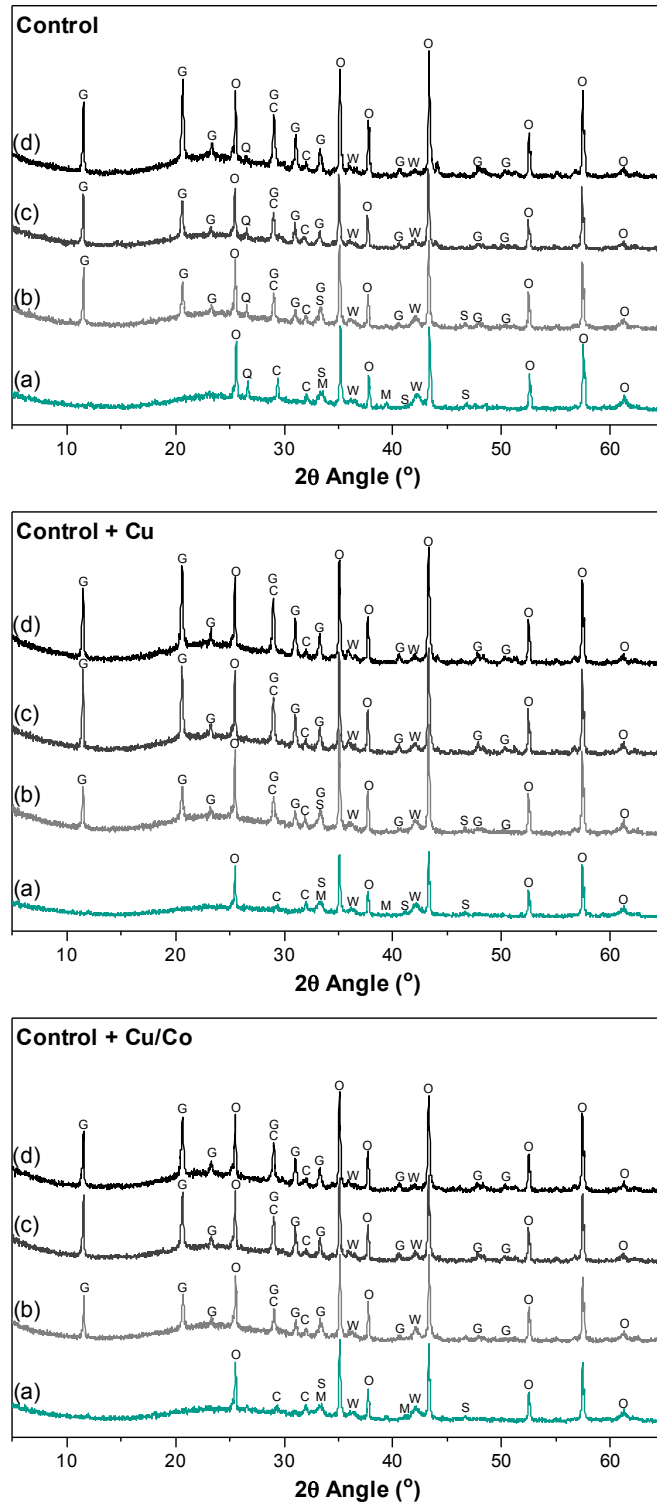
262 **Figure 3**.

Figure 4. XRD patterns for all samples exposed to increasing concentrations of sulfuric acid: (a) 0 eq, (b) 4 eq, (c) 6 eq, and (d) 8 eq. S: srebrodolskite, G: gypsum, H: calcium sulfate hydrate, C: calcium silicate hydrate (C-S-H), W: wüstite, Q: quartz, M: merwinite, O: corundum.

266   *3.3 Permeable Porosity*

267   After exposure to deionized water and sulfuric acid, all AAC materials increased in permeable porosity

268   (**Figure 5**). The Control exhibited the highest permeable porosity of all sample formulations when

269   exposed to either water or acid. When exposed to the same, samples including Cu and Co resulted in

270   lower porosities when compared to the otherwise identical Control. Comparison between Control + Cu

271   and Control + Cu/Co samples indicate no statistically significant difference in porosity upon exposure to

272   water. However, when exposed to acid, the Control + Cu/Co sample exhibited the lowest porosity overall.
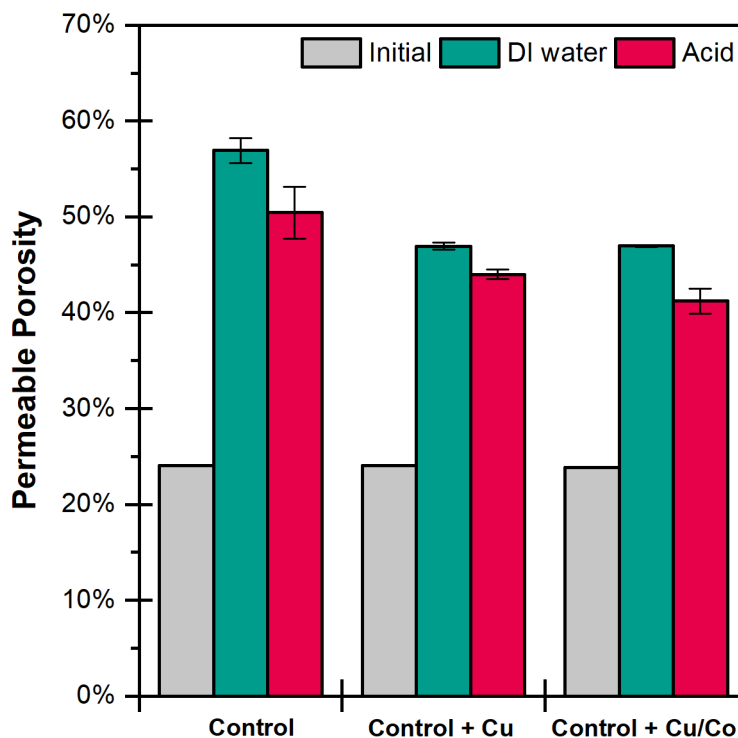
273

274   **Figure 5.** Permeable porosities after seven days of exposure in deionized water and sulfuric acid.

275   *3.4 Corrosion-Layer Depth*

276   Addition of heavy metals in AACs resulted in a decrease of the corrosion-layer depth as shown in **Figure**

277   **6**. Cu and Cu/Co, respectively, decreased the corrosion-layer depth by 8% and 17%. More specifically,

278   results demonstrate that addition of Cu/Co reduced the average depth of the weak corrosion layer by

279   approximately 26% compared to the Control samples without heavy metal addition.

280
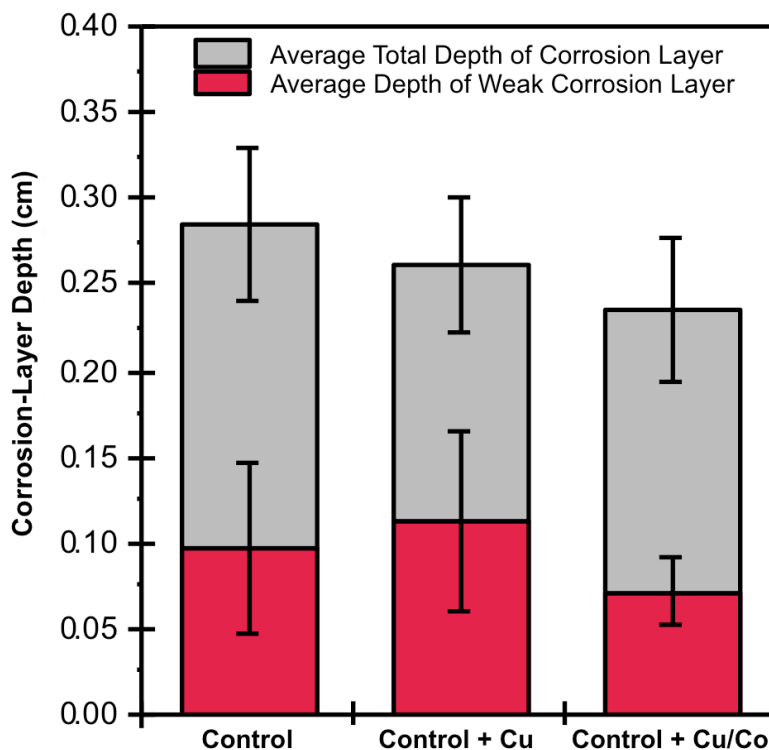
Figure 6. Corrosion-layer depth of all samples, including the thickness of weak corrosion layer, after
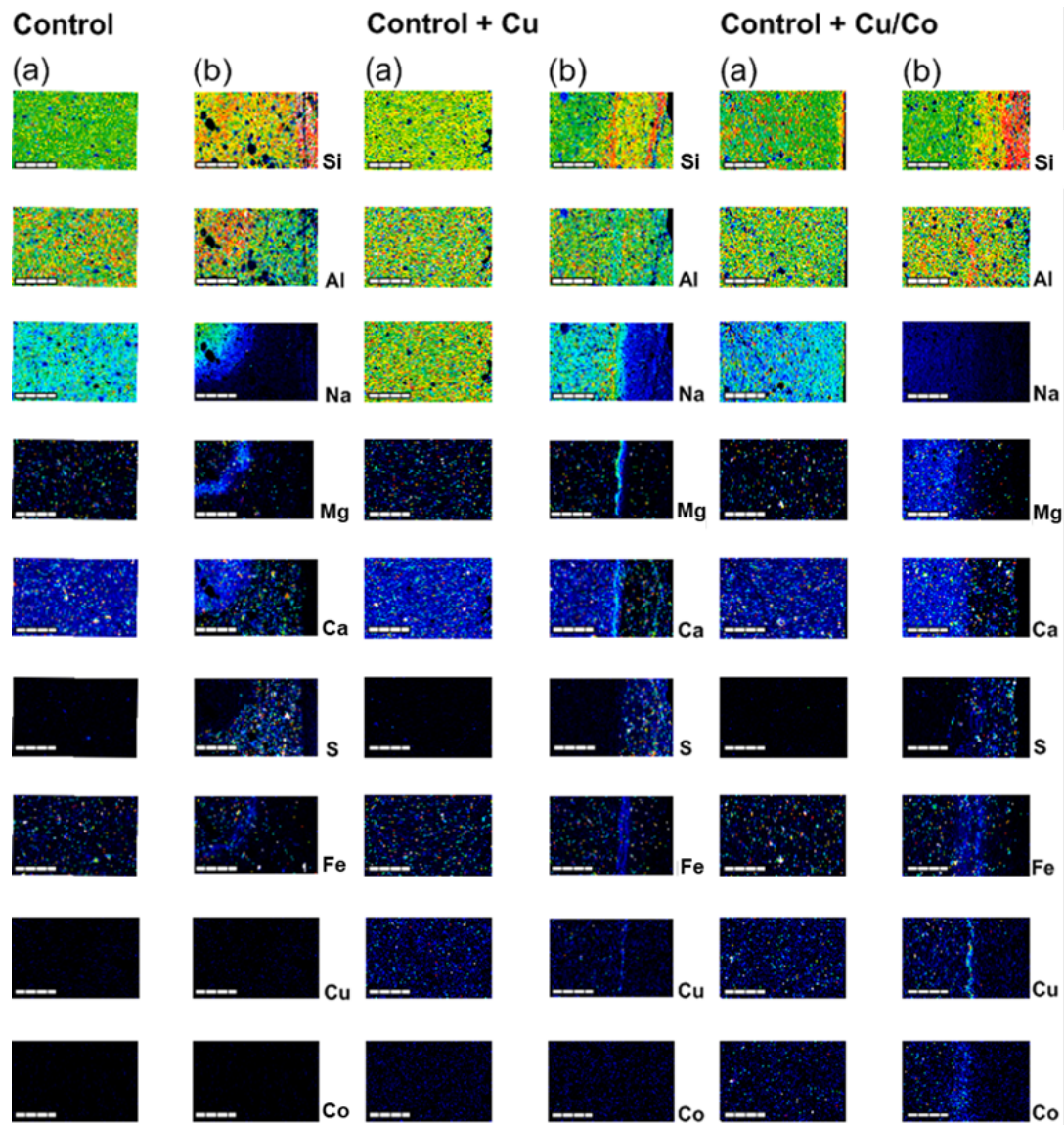seven days of exposure in sulfuric acid (n = 3).

3.5 Elemental maps of AACs exposed to acid

Elemental compositions of the AAC samples before and after seven days of sulfuric acid exposure are
shown in **Figure 7**. As shown in **Figure 7a**, all samples have an initially homogeneous distribution of
elements within the AAC microstructure before acid exposure.

After acid exposure, some similarities remain between samples (**Figure 7b**). Overlap between Ca, Fe,
and Mg net intensity counts, for example, indicate the presence of unreacted mineral phases found in the
BOF-slag precursor (see **Figure 7a**). Net elemental intensity counts between the different samples
indicate different solid phases that form in response to acid exposure (**Figure 7b**). For example, after acid
exposure, overlap between the net intensities of both Ca and sulfur (S) maps indicate precipitation of
gypsum within cracks and pores of the AAC samples, corroborating evidence from the XRD patterns. In
addition, the visually observable corrosion layer is depicted in each sample by the decalcification present
in the Ca maps (**Figure 7b**).

Despite these similarities, many notable differences between formulations are evident after acid
exposure. For instance, while acid exposure induces transience of Si and Al in all samples, the extent of
their mobility and ultimate fate differ among samples. Si-rich bands developed with more distinct

298   uniformity in samples containing Cu and Co (**Figure 7b**). Si in the Control sample is observed to form a

299   heterogeneous distribution of Si-rich areas. Dealumination (ejection of Al from the AAC binder) was

300   observed in all samples; however, as judged by elemental mapping, dealumination decreased in

301   formulations containing Cu and Co. After acid exposure, cation mobility occurred past the border of what

302   macroscopically corresponded to the corrosion layer (**Figure 7b**). While Na was observed to leach out of

303   all AAC formulations, Na redistributed past the visually observable corrosion layer in the Control and

304   Control + Cu samples, while formulations containing both Cu and Co exhibited the highest Na leaching.

305   All samples demonstrated cationic dissolution and subsequent mobility of Mg. Control and Control + Cu

306   samples presented diffuse Mg-containing bands at the visually observable corrosion front, while samples

307   containing both Cu and Co exhibited homogeneous mobility of Mg past the visually observable corrosion

308   layer. Similar to the behavior of Mg in Control samples, Fe forms a diffuse band at the visually

309   observable corrosion front, yet in samples containing both Cu and Co, Fe concentrated a double-layered

310   band at the same location. Inclusion of both Cu and Co resulted in their mobilization and formation of a

311   band at the visually observable corrosion front (**Figure 7b**). Cu, when included in any formulation,

312   created a Cu-rich band, while Co accumulated as a band in the same position albeit by lesser net intensity

313   counts compared to Cu.

314   **Figure 7.** Elemental mapping of Control, Control + Cu, Control + Cu/Co samples when (a) unexposed to

315   acid and (b) after seven days of sulfuric acid exposure. Acid intrusion direction is from right to left. Scale

316   bar = 1mm. Net-count color intensity scales are provided in the **Supplementary Information**.

317   **4. Discussion**

318   *4.1 Heavy metals modify AAC microstructure and properties*

319   Results from the desorption potential experiment indicate that a maximum of 98% of any heavy metal

320   element (i.e., Cu, Co) was liberated by the Control + Cu and Control + Cu/Co formulations after exposure

321   to 6 eq of acid (**Figure 2**). In comparison, semi-dynamic leaching revealed lower leaching of both Cu and

322   Co (**Figure 1**). The difference in leaching behavior might indicate a complex behavior of heavy metals

323   exposed to acidic conditions, which may relate to heavy metals compensating charges within the

324   aluminosilicate framework. Similar heavy metal charge-compensation has been observed in [32] and [33]

325   for multivalent heavy metals with +2 and +3 charges.

326   Heavy-metal modifications resulted in distinctive changes to material properties. All AAC samples

327   analyzed herein are composed of both C-S-H (**Figure 3** and **Figure 4**) and N-A-S-H binders. This

328   observation has been similarly observed in studies of blended systems [34] and, in this study, it is due to

329   presence of belite (**Supplementary Information**) in the slag precursor and of reactive Si and Al in the

330   metakaolin precursor (**Table 1**). The inclusion of Cu and Co increased elemental leaching of both Si and

331   Na in deionized water (**Figure 1**) as compared to the Control sample. Leaching of Si and Na ions in

332   AACs may be explained by a shift in equilibrium due to chemical reactions of free silicate monomers,

333   dimers, trimers, and alkali metals (i.e., Na), as explained by [22]. Leaching of Na from the AAC

334   microstructure allows for the breakdown and mobility of unreacted Si monomers and oligomers. As a

335   result, higher leaching of Si and Na indicate that Control + Cu and Control + Cu/Co samples may have

336   higher unreacted Si content. This finding is consistent with (1) prevailing theory that suggests that heavy-

337   metal cations (i.e., Cu, Co) aid in stabilization of negatively charged Al anions in the binder's Si-O-Al-O

338   chain, enhancing mobility of other cations (i.e., Na) [32], and (2) studies on NaSi gels with low Si

339   contents (low SiO_2/Na_2O molar ratios) that revealed higher Si leaching when exposed to deionized water

340   [35]. Finally, the addition of heavy metals reduces dealumination of AACs as evidenced by the

341   decreasing shifts in distributions of aluminum atoms (**Figure 8**) and decreased changes to the bulk Si:Al

342   ratios (**Table 5**) before and after acid exposure. Reductions in dealumination improves resistance to

343   changes in porosity due to sulfuric acid and deionized water exposure (**Figure 5**), retards gypsum

344   formation (**Figure 3** and **Figure 4**), and reduces the observable corrosion depth when exposed to acid

345   (**Figure 6**).
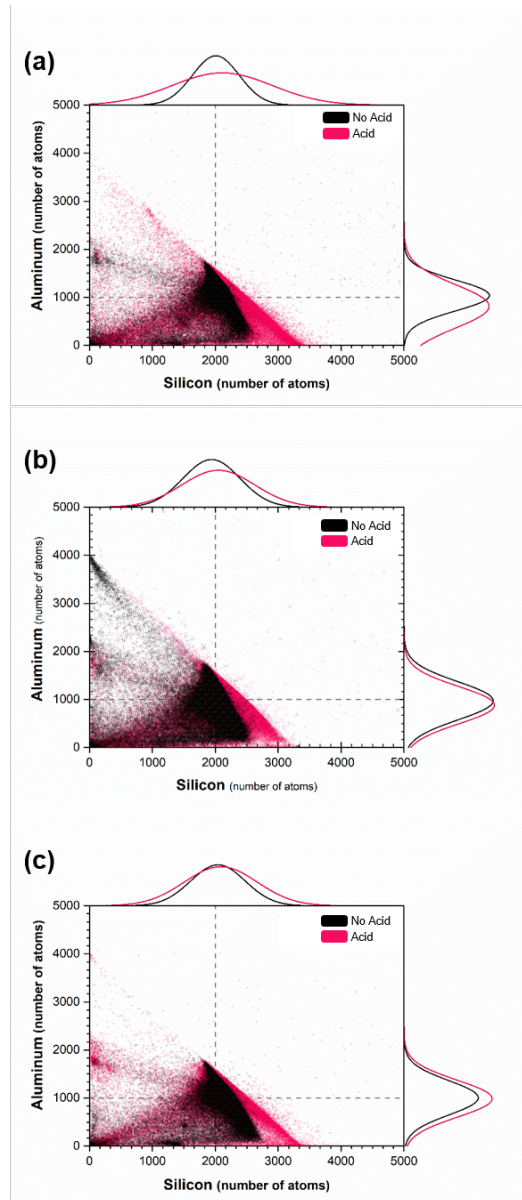
346

347 **Figure 8.** Number of silicon and aluminum atoms at each EMPA data point for (a) Control, (b) Control +

348 Cu, (c) Control + Cu/Co samples before and after acid exposure. Cross section of lines within each plot

349 indicate a Si:Al ratio of 2.0.

350

351 **Table 5.** Bulk Si:Al ratio means and medians derived from EMPA data.

Unexposed				Acid Exposed			
Sample	**Median**	**Mean**	**S.D.**	**Sample**	**Median**	**Mean**	**S.D.**
Control	1.86	1.9	0.42	Control	2.43	2.57	1.01
Control + Cu	1.97	2.02	0.51	Control + Cu	2.29	2.42	0.84
Control + Cu/Co	1.92	1.98	0.52	Control + Cu/Co	1.96	2.08	0.79

352

353   ***4.2 Dissolution and precipitation reactions due to loss of pore structure***

354   Pore structure—and the preservation of the pore solution—is hypothesized to play an important role in

355   the dissolution and precipitation reactions occurring during exposure to aggressive solutions. In this

356   study, leaching of soluble phases or inducing mobility of ions in the AAC matrix enabled different

357   mineral precipitation in acid. For example, ion dissolution yielded precipitation of gypsum when

358   powdered samples were exposed to sulfuric acid (**Figure 4**). Contrastingly, cast samples with heavy

359   metals resulted in retarded gypsum precipitation when exposed to acid (**Figure 3**). The different behavior

360   of cast samples could be explained by the retention of the pore structure and preservation of the pore

361   solution, which may reduce the initial dissolution and subsequent precipitation reactions. Similar

362   observations have been reported in [36], where fly ash-based AAC samples retaining their pore structure

363   during deionized water exposure exhibited lack of mineral formation.

364   ***4.3 Acid degradation mechanisms***

365   While evidence consistent with prevailing acid degradation theory [13], [22] was observed here—

366   dealumination and decalcification—elemental mapping analysis of acid-stressed AACs containing Cu and

367   Co indicate that other acid degradation mechanisms are possible in these materials. Differences in

368   dealumination and decalcification were observed in the presence and absence of Cu and Co (**Figure 7**).

369   For example, dealumination progressed in Control samples with the concomitant loss of Al from the

370   microstructure, while decalcification was observed in all samples. These results suggest that the presence

371   of heavy metals, such as Co and/or Cu, can influence the extent and pathways of acid degradation in the

372   following specific terms: (a) extent of H_3O^+ penetration, (b) cationic mobility, fate, and stabilization of the

373   AAC microstructure, and (c) formation of an acid passivation barrier.

374   *4.3.1 H_3O^+ penetration into the AAC framework*

375   Experimental evidence confirms H_3O^+ penetration past the visually observable corrosion layer, which may

376   be responsible for inducing cationic mobility *via* mineral dissolution. For example, elemental mapping of

377   Mg and Fe reveal mineral dissolution and subsequent cation mobility upon acid exposure past the visually

378   observable corrosion layer in any sample, as defined by the decalcification fronts observable in the Ca

379   elemental maps (**Figure 7**). In general, acid-induced mineral dissolution is caused by the presence of

380   H_3O^+ ions and their adsorption onto solid surfaces. The H_3O^+-induced dissolution of Mg- and Fe-

381   containing minerals observed herein (**Figure 3**) is likely similar to the dissolution of forsterite, a

382   magnesium silicate mineral. In acid-induced forsterite dissolution, three hydrogen atoms of an hydronium

383   ion dissolve the mineral by associating with two bridging oxygen atoms and liberating the Mg cation [37].

384   Furthermore, other studies have validated the role of H_3O^+ ions on the dissolution of Fe-containing

385   mineral phases [38]. Therefore, given that H_3O^+ ions play an important role in the occurrence and rate of

386   both Mg- and Fe-containing mineral dissolution [39], its deeper presence within the aluminosilicate

387   framework indeed would induce both mineral dissolution and cationic mobility.

388   *4.3.2 Cationic mobility, fate, and stabilization of AAC microstructure*

389   Results indicate that the mobility of cations (e.g., Mg, Fe) within the microstructure may influence the

390   leaching of other cations (e.g., Na). When exposed to sulfuric acid, Cu/Co-containing samples leached the

391   most Na of all AACs (**Figure 1**). Complementary to these results, **Figure 7b** indicates the absence of Na

392   in corroded regions. Absence of Na charge-balancing cations may be exacerbated by the mobility of other

393   cations within the microstructure, such as Mg from merwinite minerals **(Figure 3)**, and potential binder

394   charge-compensation by Cu and Co, as explained previously. For example, the quantity of free Mg

395   cations can be observed to increase in areas of high Na leaching (**Figure 7b**). Furthermore, in samples

396   incorporating Cu and Co, the release of Na atoms may be preferential in these samples and, also, may not

397   compromise acid resistance due to extensive cationic mobility of Mg, as further discussed in the

398   following paragraph. These observations not only further provide evidence of cationic mobility past the

399   visually observable corrosion layer, but also help explain the findings reported in [39], which show that

400   high alkali contents improve the acid resistance of AACs.

401   Cationic dissolution from minerals (**Figure 3**) and subsequent retention of cations within the AAC

402   framework stabilizes the binder and prevents further deterioration in acid. As previously discussed, Mg

403   elemental maps (**Figure 7**) show the dissolution of Mg mineral phases (merwinite) past the visually

404   observable corrosion depth (decalcified front).At these same depths, cation mobility is also observed in

405   samples incorporating Cu and Co. These heavy metal-containing samples exhibit lower porosity changes

406   after acid challenges and yield lower amounts of corrosion product as judged by caliper measurements

407   (see **Figure 5** and **Figure 6**). Based on these results, it is hypothesized that the released cations may act as

408   replacements for the initial charge-balancing cations (primarily Ca and Na), whose weak bonds with Al in

409   the binder can be replaced by hydronium ions penetrating the AAC matrix [40]. In this context, the

410   inclusion of diffusible Cu and Co as supplementary cations appear to play an important role in inhibiting

411   electrophilic attack of AAC binders by H_3O^+ ions [17].

412   *4.3.3 Passivation barrier formation*

413   Fe, Cu, and Co cations appear to form a passivation barrier, which may help reduce the extent of

414   dealumination and improve the acid resistance of AACs. After seven days of acid exposure, AAC

415   samples with heavy metals concentrated in bands with other cations at the degradation front (see **Figure**

416   **7**). Complementary to these results, these samples exhibited the lowest porosity changes and smallest

417   corrosion depth compared to the otherwise identical Control samples (**Figure 5**, **Figure 6**). These

418   observations are novel, as the role of Fe in AACs, and, especially, their role in acid degradation, has not

419   been fully explored, with only limited studies demonstrating reductions in the local Fe coordination after

420   alkali activation [41]–[43].

421   The proposed mechanism of acid degradation is illustrated in **Figure 9**. Complementary to existing

422   acid degradation theory, the presence of a passivation barrier is hypothesized to create different pH and

423   silica concentration conditions within the AAC microstructure, which affect the stability of silica gels in

424   acidic conditions. During acid challenges, electrophilic attack of Si-O-Al bonds by H_3O^+ ions (**reaction 1**)

425   [13], and subsequent decalcification results in dealumination (**reaction 2a**). Given the data presented in

426   this study, it is evidenced that dealumination competes with a process of cation stabilization (Mg^{+2}, Fe^{+3},

427   Ca^{+2}), as presented in **reaction 2b** and demonstrated by **Figure 7**. After dealumination, formation of a

428   protective layer of polymerized silica has been observed (**reaction 3a**) [44]; this gel is believed to be less

429   porous and aids in the retention of cations, promoting acid resistance. Previously, a set of balanced

430   equilibrium reactions was proposed to describe the polymerization of silica species and subsequent

431   formation of silica gels at low pH values [22]. However, the polymerization and, later, gelation of silica

432   species is a pH- and concentration-dependent process based on chemical equilibrium, which has not been

433   previously considered in [22]. The fundamental chemistry of silica has previously been explained in detail

434   [45], where polymerization of silica at pH 2-7 is described in the following steps: (1) polymerization of

435   silica monomers (orthosilicic acid) to dimers, trimers, cyclic oligomers, and particles, (2) slow particle

436   growth reaching a diameter of 2-3 nm, and (3) collision or aggregation of silica particles into chains and

437   then gel networks. The aforementioned steps are limited by the concentration of orthosilicic acid

438   monomers in solution, which, if maintained above its solubility concentration limit, permits silica

439   polymerization and particle growth, as described by nucleation theory [46] (**reaction 3b**).

440
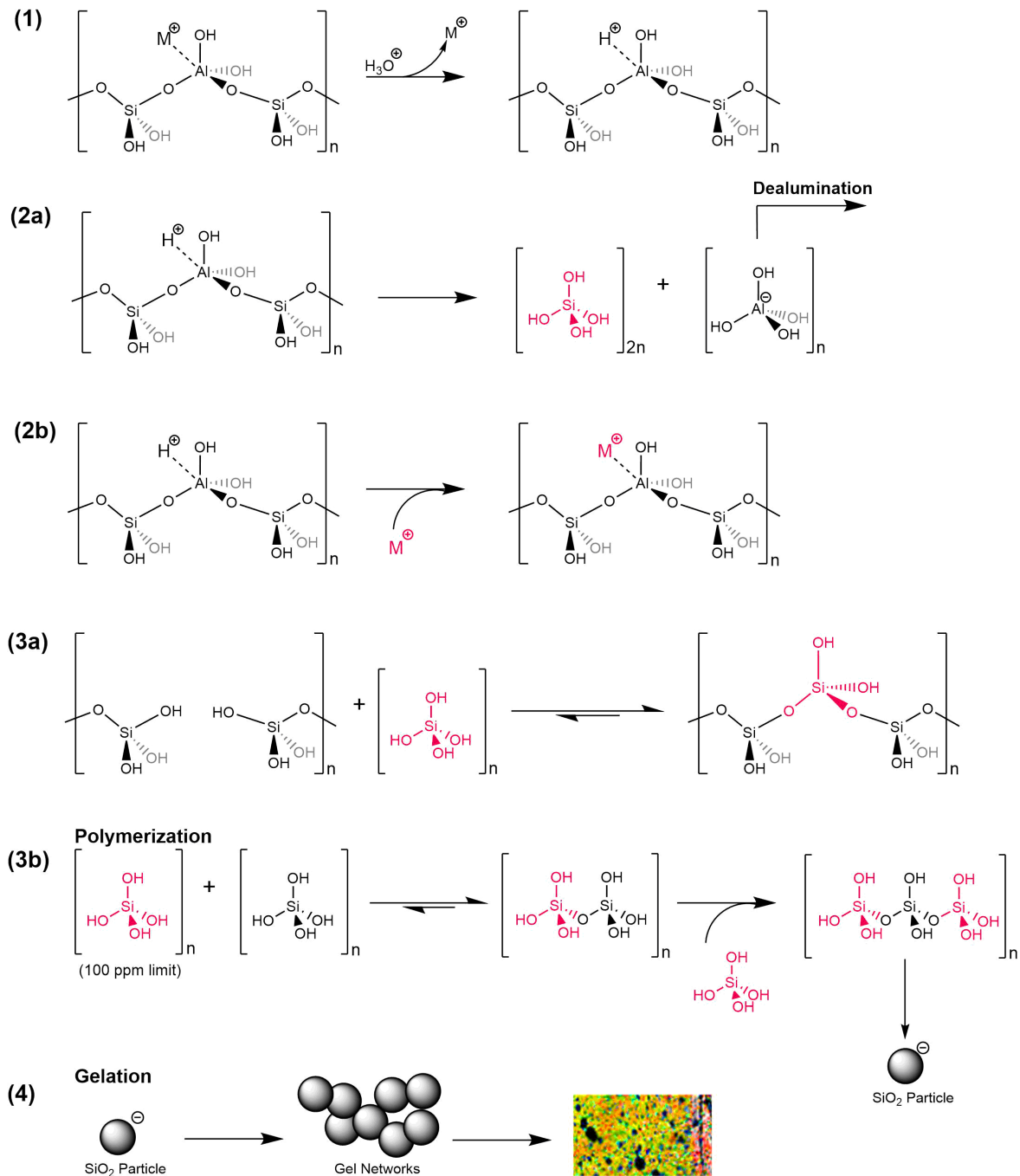
Figure 9. Proposed mechanism of acid degradation.

The presence of multivalent cations (Mg^{+2}, Fe^{+3}, Ca^{+2}, Co^{+2}, Cu^{+2}) within the AAC microstructure affects both (1) the stability of silica species and (2) pH conditions, which may be further promoted via creation of the passivation barrier. As a result, these two concurrent conditions may permit the formation of stratified silica gels. Evidence, presented in [44], demonstrates the ability of heavy metals in solution to favor the stability of polymeric silica species and retard depolymerization into orthosilicic monomers. The

449   higher stability of polymeric silica species may enhance silica mobility to the periphery of AAC samples

450   as facilitated by diffusion (**Figure 7**). Subsequently, depending on the concentration, the presence of

451   multivalent cations (Mg^{+2}, Fe^{+3}, Ca^{+2}, Co^{+2}, Cu^{+2}) decreases the rate and size of silica particle aggregation

452   due to silica particle stabilization, as described in [45]–[47]. The semi-dynamic leaching data, presented

453   in **Figure 1**, demonstrates lower leaching of multivalent cations. These results suggest that particle

454   aggregation size and rate is decreased, which may further enhance the mobility of smaller silica particle

455   aggregates to the periphery of the material. As silica species mobilize to the periphery, if the pH within

456   the AAC microstructure is lower, then polymerization of silica monomers (**reaction 3b**) and gelation of

457   silica particles (**reaction 4**) is expected to increase, as described in [48], [49]. Additionally, the former

458   two conditions (silica stability and pH) may be further maintained by the formation of the passivation

459   barrier, thus, aiding the stratified formation of silica gels at the periphery (**Figure 7**). Benefiting the acid

460   resistance of AACs, the formation of silica gels may serve as an adequate protective, non-porous, and

461   impermeable layer [50]. Inversely, in AAC samples without heavy metals, previously mentioned pH or

462   silica conditions may not be present due to the lower content of multivalent cations and absence of a

463   passivation barrier. Instead, sporadic and randomized gelation may be preferred throughout the AAC

464   microstructure (**Figure 7**). In summary, the experimental evidence presented here suggests an alternate

465   pathway for the formation of a stratified silica-rich gel in the presence of heavy metals during acid

466   degradation– one that depends on the presence of multivalent cations, pH conditions, and silica

467   speciation.

468

469   **5. Conclusion**

470   The aim of this study was to investigate the effect of heavy metals, namely copper (Cu) and cobalt (Co),

471   on the acid resistance of AACs. In this study, adsorption of Cu and Co onto a basic oxygen furnace slag

472   (BOF-S) precursor improved the acid resistance of binary metakaolin and BOF-S-based AACs.

473   This study resulted in the following significant findings:

474   1.   AACs micro-doped with Cu and Co inhibited the rate of calcium sulfate mineral formation,

475   resulting in lower permeable porosities and smaller corrosion depths;

476   2.   Hydronium ions were evident within the AAC framework and extended beyond the visually

477   observable corrosion front;

478   3.   Hydronium ion penetration was associated with increased cation mobility; mobile cations aided in

479   the stabilization of cementitious binders;

480   4.   Fe, Cu, and Co ions formed passivation barriers at the acid degradation front, suggesting they

481   play a critical role in reducing the extent of dealumination and improving the acid resistance of

482   AACs;

483   5. A stratified silica-rich gel was observed in AACs containing Cu and Co; the formation of this gel

484   is likely dependent on the presence of multivalent cations, pH conditions, and silica speciation.

485 Together, these data provide new experimental evidence of a more complex AAC acid degradation

486 mechanism than previously observed.

6. Acknowledgments

7. References

497 [1]   B. Huber, H. Hilbig, J. E. Drewes, and E. Muller, "Evaluation of concrete corrosion after short-

498   and long-term exposure to chemically and microbially generated sulfuric acid," *Cem. Concr. Res.*,

499   vol. 94, pp. 36–48, 2017.

500 [2]   U.S. Environmental Protection Agency (EPA), "Clean Watersheds Needs Survey - Report to

501   Congress," 2008.

502 [3]   American Society of Civil Engineers (ASCE) Foundation, "2017 Wastewater Infrastructure Report

503   Card," 2017.

504 [4]   C. Grengg, F. Mittermayr, A. Baldermann, M. E. Bottcher, A. Leis, G. Koreimann, and M.

505   Dietzel, "Bacteriogenically Induced Sulfuric Acid Attack on Concrete in an Austrian Sewer

506   System," in *XIII Conference on Durability of Building Materials and Components*, 2017, pp. 897–

507   903.

508 [5]   C. D. Parker, "Mechanics of Corrosion of Concrete Sewers by Hydrogen Sulfide," *Sewage Ind.*

509   *Waste.*, vol. 23, no. 12, pp. 1477–1485, 1951.

510 [6]   A. L. Ling, C. E. Robertson, J. K. Harris, D. N. Frank, C. V. Kotter, M. J. Stevens, N. R. Pace, and

511   M. T. Hernandez, "High-resolution microbial community succession of microbially induced

512   concrete corrosion in working sanitary manholes," *PLoS One*, vol. 10, no. 3, pp. 1–12, 2015.

513 [7]   J. Vollertsen, A. H. Nielsen, H. S. Jensen, T. Wium-Andersen, and T. Hvitved-Jacobsen,

514   "Corrosion of concrete sewers-The kinetics of hydrogen sulfide oxidation," *Sci. Total Environ.*,

515   vol. 394, no. 1, pp. 162–170, 2008.

516 [8]   R. Sterling, J. Simicevic, E. Allouche, W. Condit, and L. Wang, "State of Technology for

517   Rehabilitation of Wastewater Collection Systems," 2010.

518   [9]   E. Hewayde, M. L. Nehdi, E. Allouche, and G. Nakhla, "Using concrete admixtures for sulphuric

519   acid resistance," *Proc. Inst. Civ. Eng. - Constr. Mater.*, vol. 160, no. 1, pp. 25–35, 2007.

520   [10]   W. De Muynck, N. De Belie, and W. Verstraete, "Effectiveness of admixtures, surface treatments

521   and antimicrobial compounds against biogenic sulfuric acid corrosion of concrete," *Cem. Concr.*

522   *Compos.*, vol. 31, no. 3, pp. 163–170, 2009.

523   [11]   B. Hashemi, T. Iseley, and J. Raulston, "Water Pipeline Renewal Evaluation Using AWWA Class

524   IV CIPP, Pipe Bursting, and Open-Cut," in *ICPTT 2011 ASCE*, 2011, pp. 1257–1266.

525   [12]   C. Shi, A. F. Jiménez, and A. Palomo, "New cements for the 21st century: The pursuit of an

526   alternative to Portland cement," *Cem. Concr. Res.*, vol. 41, no. 7, pp. 750–763, 2011.

527   [13]   A. Allahverdi and F. Škvára, "Sulfuric acid attack on hardened paste of geopolymer cements-Part

528   1. Mechanism of corrosion at relatively high concentrations," *Ceram. - Silikaty*, vol. 49, no. 4, p.

529   225, 2005.

530   [14]   A. Allahverdi and F. Škvára, "Sulfuric acid attack on hardened paste of geopolymer cements Part

531   2. Corrosion mechanism at mild and relatively low concentrations," *Ceram. - Silikaty*, vol. 50, no.

532   1, pp. 1–4, 2006.

533   [15]   A. Allahverdi and F. Škvára, "Nitric acid attack on hardened paste of geopolymeric cements. Part

534   2," *Ceram. - Silikaty*, vol. 45, no. 4, pp. 143–149, 2001.

535   [16]   A. Allahverdi and F. Škvára, "Nitric acid attack on hardened paste of geopolymeric cements. Part

536   1.," *Ceram. - Silikaty*, vol. 45, no. 4, pp. 143–149, 2001.

537   [17]   A. Allahverdi and F. Škvára, "Acid Corrosion of Geopolymeric Cements," in *Seventh*

538   *CANMET/ACI International Conference on fly ash, silica fume, and natural pozzolans in concrete*,

539   2001, vol. 2, pp. 561–579.

540   [18]   S. A. Bernal, E. D. Rodríguez, R. Mejía, R. Mejía De Gutiérrez, and J. L. Provis, "Performance of

541   alkali-activated slag mortars exposed to acids Performance of alkali-activated slag mortars

542   exposed to acids," *J. Sustain. Cem. Mater.*, vol. 1, no. 3, 2012.

543   [19]   T. Bakharev, J. G. Sanjayan, and Y. B. Cheng, "Resistance of alkali-activated slag concrete to acid

544   attack," *Cem. Concr. Res.*, vol. 33, no. 10, pp. 1607–1611, 2003.

545   [20]   C. Shi and J. . A. Stegemann, "Acid corrosion resistance of different cementing materials," *Cem.*

546   *Concr. Res.*, vol. 30, no. 5, pp. 803–808, 2000.

547   [21]   M. A. M. Ariffin, M. A. R. Bhutta, M. W. Hussin, M. M. Tahir, and N. Aziah, "Sulfuric acid

548   resistance of blended ash geopolymer concrete," *Constr. Build. Mater.*, vol. 43, pp. 80–86, 2013.

549   [22]   T. Bakharev, "Resistance of geopolymer materials to acid attack," *Cem. Concr. Res.*, vol. 35, no.

550   4, pp. 658–670, 2005.

551   [23]   R. Sathia, K. Ganesh Babu, and M. Santhanam, "Durability Study of Low Calcium Fly Ash

552   Geopolymer Concrete," in *The 3rd ACF International Conference- ACF/VCA*, 2008, pp. 1153–

553   1159.

554   [24]   F. Pacheco-Torgal, Z. Abdollahnejad, a. F. Camões, M. Jamshidi, and Y. Ding, "Durability of

555   alkali-activated binders: A clear advantage over Portland cement or an unproven issue?," *Constr.*

556   *Build. Mater.*, vol. 30, pp. 400–405, 2012.

557   [25]   A. Caicedo-Ramirez, A. L. Ling, and M. Hernandez, "Diffusion susceptibility demonstrates

558   relative inhibition potential of sorbent-immobilized heavy metals against sulfur oxidizing

559   acidophiles," *J. Microbiol. Methods*, vol. 131, pp. 42–44, 2016.

560   [26]   R. F. Farrell, S. A. Matthes, and A. J. Mackie, "A simple, low-cost method for the dissolution of

561   metal mineral samples in plastic pressure vessels," *U.S. Bur. Mines Rep.*, no. BM-RI-8480, p. 19,

562   1980.

563   [27]   M. Torres-Carrasco and F. Puertas, "Waste glass in the geopolymer preparation. Mechanical and

564   microstructural characterisation," *J. Clean. Prod.*, vol. 90, pp. 397–408, 2015.

565   [28]   D. D. Eberl, "User Guide to RockJock- A program for determining quantitative mineralogy from

566   X-ray diffraction Data," *U.S. Geol. Surv. Open-File Rep.*, p. 47, 2003.

567   [29]   M. Safiuddin and N. Hearn, "Comparison of ASTM saturation techniques for measuring the

568   permeable porosity of concrete," *Cem. Concr. Res.*, vol. 35, no. 5, pp. 1008–1013, 2005.

569   [30]   J. J. Donovan and T. N. Tingle, "An improved mean atomic number background correction for

570   quantitative microanalysis," *Microsc. Microanal.*, vol. 2, no. 1, pp. 1–7, Feb. 1996.

571   [31]   J. Goldstein, D. Newbury, D. Joy, C. Lyman, P. Echlin, E. Lifshin, L. Sawyer, and J. Michael,

572   *Scanning Electron Microscopy and X-Ray Microanalysis*, 3rd ed., vol. 53, no. 9. Springer

573   Science+Business Media, LLC, 2013.

574   [32]   F. Škvára, L. Kopecky, V. Smilauer, and Z. Bittnar, "Material and structural characterization of

575   alkali activated low-calcium brown coal fly ash," *J. Hazard. Mater.*, vol. 168, pp. 711–720, 2009.

576   [33]   N. Waijarean, K. J. D. Mackenzie, S. Asavapisit, R. Piyaphanuwat, and G. N. L. Jameson,

577   "Synthesis and properties of geopolymers based on water treatment residue and their

578   immobilization of some heavy metals," *J. Mater. Sci.*, vol. 52, no. 12, pp. 7345–7359, 2017.

579   [34]   J. L. Provis and J. S. J. van Deventer, "Alkali Activated Materials, State-of-the-Art Report,

580   RILEM TC 224-AAM," Springer US, 2014.

581   [35]   D. Dimas, I. Giannopoulou, and D. Panias, "Polymerization in sodium silicate solutions: A

582   fundamental process in geopolymerization technology," *J. Mater. Sci.*, vol. 44, no. 14, pp. 3719–

583   3730, 2009.

584   [36]   A. Fernandez-Jimenez, I. García-Lodeiro, and A. Palomo, "Durability of alkali-activated fly ash

585   cementitious materials," *J. Mater. Sci.*, 2007.

586   [37]   J. J. Rosso and D. J. Rimstidt, "A high resolution study of forsterite dissolution rates," *Geochim.*

587   *Cosmochim. Acta*, vol. 64, no. 5, pp. 797–811, 2000.

588   [38]   D. Baron and C. D. Palmer, "Solubility of KFe3 (CrO4)2(OH)6 at 4 to 35 °C," *Geochim.*

589   *Cosmochim. Acta*, vol. 60, no. 20, pp. 3815–3824, 1996.

590   [39]   S. A. Carroll-Webb and J. V Walther, "A surface complex reaction model for the pH-dependence

591   of corundum and kaolinite dissolution rates," *Geochim. Cosmochim. Acta*, vol. 52, pp. 2609–2623,

592   1988.

593   [40]   F. Škvára, V. Šmilauer, P. Hlavácek, L. Kopecky, and Z. Cilová, "A Weak Alkali Bond in (N,K)-

594   A-S-H Gels: Evidence from Leaching and Modeling," *Ceram. − Silikáty*, vol. 56, no. 4, pp. 374–

595   382, 2012.

596   [41]   S. Noor, H. Guy, N. L. J. Joanne, and K. J. D. Mackenzie, "Synthesis and properties of inorganic

597   polymers (geopolymers) derived from Bayer process residue (red mud) and bauxite," *J. Mater.*

598   *Sci.*, vol. 50, no. 23, pp. 7713–7724, 2015.

599   [42]   D. S. Perera, J. D. Cashion, M. G. Blackford, Z. Zhang, and E. R. Vance, "Fe speciation in

600   geopolymers with Si/Al molar ratio of ~2," *J. Eur. Ceram. Soc.*, vol. 27, no. 7, pp. 2697–2703,

601   2007.

602   [43]   P. N. Lemougna, K. J. D. MacKenzie, G. N. L. Jameson, H. Rahier, and U. F. Chinje Melo, "The

603   role of iron in the formation of inorganic polymers (geopolymers) from volcanic ash: A 57Fe

604   Mossbauer spectroscopy study," *J. Mater. Sci.*, vol. 48, no. 15, pp. 5280–5286, 2013.

605   [44]   M. Dietzel, "Dissolution of silicates and the stability of polysilicic acid," *Geochim. Cosmochim.*

606   *Acta*, vol. 64, no. 19, pp. 3275–3281, 2000.

607   [45]   R. K. Iler, *Chemistry of Silica - Solubility, Polymerization, Colloid and Surface Properties and*

608   *Biochemistry*. Hoboken, NJ: John Wiley & Sons, 1979.

609   [46]   P. W. J. G. Wijnen, T. P. M. Beelen, and R. A. Van Santen, "Silica Gels from Aqueous Silicate

610   Solutions," in *The Colloid Chemistry of Silica*, vol. 234, American Chemical Society, 1994, pp.

611   26–517.

612   [47]   F. Gaboriaud, D. Chaumont, A. Nonat, B. Hanquet, and A. Craeivich, "Study of the Influence of

613   Alkaline Ions (Li, Na and K) on the Structure of the Silicate Entities in Silico Alkaline Sol and on

614   the Formation of the Silico-Calco-Alkaline Gel," *J. Sol-Gel Sci. Technol.*, vol. 13, no. 1–3, p. 353,

615   1998.

616   [48]   J. Nordström, E. Nilsson, P. Jarvol, M. Nayeri, A. Palmqvist, J. Bergenholtz, and A. Matic,

617   "Concentration- and pH-dependence of highly alkaline sodium silicate solutions," *J. Colloid*

618   *Interface Sci.*, vol. 356, no. 1, pp. 37–45, 2011.

619   [49]   C. O. Metin, L. W. Lake, C. R. Miranda, and Q. P. Nguyen, "Stability of aqueous silica

620   nanoparticle dispersions," *J. Nanoparticle Res.*, vol. 13, no. 2, pp. 839–850, 2011.

621   [50]   M. M. Komljenovic, Z. Bascarevic, N. Marjanovic, and V. Nikolic, "Decalcification resistance of

622   alkali-activated slag," *J. Hazard. Mater.*, vol. 234, pp. 112–121, 2012.

623